Influence of swift heavy ion irradiation on sensing properties of nickel-(NRs-Ni$_3$HHTP$_2$) metal-organic framework

Nikesh N. Ingle[1], Sumedh Shirsat[2], Pasha Sayyad[1], Gajanan Bodkhe[1], Harshada Patil[1], Megha Deshmukh[1], Manasi Mahadik[1], Fouran Singh[3], and Mahendra Shirsat[1,*] [ID]

[1] *RUSA Centre for Advanced Sensor Technology, Department of Physics, Dr. Babasaheb Ambedkar Marathwada University, Aurangabad, MS 431004, India*

[2] *Department of Electronics & Telecommunication Engineering, Jawaharlal Nehru Engineering College, Aurangabad, MS 431 001, India*

[3] *Inter University Accelerator Centre (IUAC), New Delhi 110 067, India*

ABSTRACT

Repercussion of Swift Heavy Ion (SHI) irradiation on nickel-based nanorods of Metal-Organic Framework (NRs-Ni$_3$HHTP$_2$ MOF) for enhancement in the properties of ChemFET-based gas sensor has been investigated. Nanorods of Ni$_3$HHTP$_2$-MOF were synthesized by chemical method and exposed to C^{12+} ions irradiation with fluence 1×10^{11} ion/cm^2 and 1×10^{12} ion/cm^2. The structural, spectroscopic, morphological, and optical characterizations were carried out using x-ray diffraction (XRD), fourier transfer infrared spectroscopy (FTIR), atomic force microscopy (AFM) with scanning electron microscopy (SEM), and UV-visible spectroscopy, respectively, whereas the bandgap was calculated from the Tauc's plot. The synthesized nanorods of Ni$_3$HHTP$_2$ MOF were drop-casted on gold-coated microelectrodes on silicon/silicon dioxide (Si/SiO$_2$) substrate, where silicon layer serves as a gate and gold microelectrodes on silicon/silicon dioxide (Si/SiO$_2$) substrate as a source and drain. The transmutations in material properties due to SHI irradiations were serviceable for enhancing field-effect transistor (transfer and output) properties and sensing properties. After Swift Heavy Ion (SHI) irradiation (1×10^{11} ion/cm^2), it shows excellent response and recovery time i.e., 20 and 23 s, respectively, for 1 ppm SO$_2$ concentration at room temp (RT) with a lower detection limit of 0.625 ppm.

Nikesh N. Ingle, Sumedh Shirsat, and Pasha Sayyad have contributed equally to this work.

Address correspondence to E-mail: mdshirsat@gmail.com

Springer

1 Introduction

In the last few years, the Metal-organic framework (MOF) is one of the focusing materials in the research world due to its tunable properties. MOFs are ultra-high porous, large surface area, highly crystalline, and high-stability material and importantly it can be tunable by altering central metal or organic ligands [1–4]. MOFs are helpful in various applications like gas storage, sensor, chemical separations, biomedical imaging, catalysis, and drug delivery as precursors for cooking graphite and metal oxides materials [1, 2, 5, 6].

The most critical problem in front of modern society is a continuous increment in pollutions in terms of air, water, sound etc [7–9]. Among these air pollution absorbed through the respiratory system. Above permissible exposure limit (PEL), hazardous gases are immediately life-threatening [10]. Sulfur dioxide is one of the responsible gases for increasing cardiorespiratory mortality and morbidity in human beings as well as the creation of corrosion in nonliving things [10, 11]. Therefore, researchers have been focusing on enhancing sensing properties of detectors for detection of various gases including SO_2 [12–15]. Since last few years, MOF has been one of the mostly explored materials for detection of various gases including SO_2. M. Tchalala [16] et al. reported fluorinated metal-organic frameworks (MOFs) used for the selective removal and sensing of SO_2 analytes. Therefore, screening of new materials and their modification for enhancing sensing properties are continuous process in the research area.

Since the last few decenniums, sundry materials have been modified extensively by high energy particles (electron, proton) of heavy ions [17–21]. The irradiation of energetic ion beams engenders several types of defects in materials like chain scission, ionization, or excitation and ion track formation etc. The Swift Heavy Ion (SHI) irradiation is one of the promising implements for material modifications and workable for enhancing electrical properties [22–25]. Zhang et al. [23] studied the performance of SHI-irradiated $MoSe_2$ material. The electrical changes were observed by using TMDC-channel field-effect transistors (FETs). Zeng et al. [26] explored the effects of electrical properties in graphene devices by exposing it to energetic ion beam irradiation where graphene was irradiated by 1.79 GeV Ta ions. It was observed that SHI-irradiated graphene at lower fluence exhibited optimized field-effect transistors performance, whereas at higher fluence, devices were significantly depreciated of electrical properties after the irradiation process. Also, Manikanthababu et al. [27] reported electrical characterization of vertical Schottky barrier diodes (SBDs) based on Ag ion-irradiated Ni/β-Ga_2O_3 materials with 120 MeV.

To date, researchers have explored SHI irradiation for modification of properties of various materials like Conducting Polymers (CPs), Single-Walled Carbon Nanotubes (SWNTs), Graphene (Gr), Metal Oxides (MOs) etc. by using various SHI and fluence rate [28–31]. Researchers have also explored SHI irradiation on various MOF materials. R. Dutta et al. [32] have reported SHI irradiation on NiBTC MOF using 100 MeV O^{7+}, which exhibited enhancement in electrochemical sensing properties. Recently, P. Sayyad et al. [33] studied the effect of Au ion with 100 MeV at fluence 1×10^{11} ion/cm^2 and 1×10^{12} ion/cm^2 irradiation on FeBTC MOF. They observed drastic changes for higher ion fluence rate. Moreover, decrease in crystallite size, increase of energy bandgap, decrease in average surface roughness, and new functional group (C–H) were observed after SHI irradiation at a higher fluence 1×10^{12} ion/cm^2.

Recently, we have explored nickel-based NRs-Ni_3-$HHTP_2$ MOF for detection of sulfur dioxide (SO_2) using ChemFET modality [34]. However, to the best of our knowledge, the influence of SHI irradiation for enhancing properties of materials for ChemFET sensing has not been explored so far. In the present work, SHI irradiation has been explored to enhance the ChemFET sensing properties of NRs-Ni_3HHTP_2 MOF using C^{12+} ion with fluence rate 1×10^{11} and 1×10^{12} ion/cm^2 irradiations. The carbon ions exhibited a distinguishable energy distribution in depth, which is known as the "Bragg Peak". Therefore, the majority of energy is released in the target [35], which will be very much useful to create defects in sensing materials. The influence of irradiation on the NRs-Ni_3HHTP_2 MOF was investigated by using structural analysis, surface morphological, electrical, and optical properties.

2 Experimental details

2.1 Fabrication of microelectrode

The device platform was prepared by using a typical photolithography process as reported earlier [36]. Highly boron (B)-doped silicon (Si) substrate having p-type nature with thickness 525 μm performed as a back gate terminal in FET measurement. A 100-nm-thick SiO_2 layer was deposited on the Si substrate by low-pressure chemical vapor deposition. It is followed by deposition of Cr layer (20 nm) and Au layer (120 nm) by e-beam evaporator and standard lift-off technique. The width of Au microelectrodes was 200 μm and the gap between two microelectrodes was 3 μm. Later micropatterned substrates were immersed in piranha solution (70% concentration $H_2SO_4/30\%H_2O_2$) followed by rinsing and drying under N_2 flow before use.

2.2 Synthesis of NRs-Ni$_3$HHTP$_2$ MOF

Nickel (II) acetate (tetrahydrate) (99.99%, purchased from Sigma Aldrich) was used without further purification along with 2,3,6,7,10,11-Hexahydroxytripenylne Hydrate (HHTP) (98%, purchased from TCI) followed by earlier reported [34]. The chemical method followed for synthesis of NRs-Ni$_3$HHTP$_2$ MOF is as follows: 2.63 mmol nickel (II) acetate (tetrahydrate) was continuously stirred with 4ml deionized water using 5ml beaker. Further addition of 1.31 mmol HHTP in continuously stirred chemical with constant heating at 80 °C for 8 h was provided. After 8 h, solution become thicker than initial solution.

The chemically synthesized NRs-Ni$_3$HHTP$_2$ solution was drop-casted to create channel in between two gold microelectrodes which was dried in room atmospheric conditions. The gold microelectrodes work as a source and drain, whereas drop-casted material create channel between them and Si substrate performed as a back gate terminal in FET measurement. For experimental test, 6 sensor devices were prepared.

2.3 SHI irradiation

The SHI irradiation was carried out by using material science beamline, 15UD Pelletron tandem accelerators at the Inter-University Accelerator Center, New Delhi, India. The scanning area of ion irradiation was $1 \times 1cm^2$ of devices riding on a ladder which was placed in the irradiated vacuum chamber under 10^{-6} mbar pressure. The targeted material was irradiated with C^{12+} ion with 50 MeV at 1pnA for fluence 1×10^{11} ion/cm^2 (16 s.) and 1×10^{12} ion/cm^2(160 s.).

The values of electronic stopping, nuclear stopping, and range of ions in NRs-Ni$_3$HHTP$_2$ were calculated by using the SRIM simulator program. The calculated values were 1647 eV/Å, 10.84 eV/Å, and 10.25 μm, respectively.

2.4 Material characterizations

The X-ray diffraction (XRD) was carried out using Bruker D8 Advance having potential difference 40 kV and current 40 kA with source CuKα (wavelength 1.5406Å). The FTIR spectrum was recorded using Bruker Alpha ATR. For surface morphology, Scanning Electron Microscopy (SEM) and Atomic Force Microscopy (AFM) were carried out by Tescan MIRA 3 LMH and Park XE-7 instruments, respectively, and UV-Vis spectroscopy was done by using Jasco V-750. FET measurements were carried out using Keithley 4200 A semiconductor parameter analyzer (SPA).

Sensing measurements were performed using indigenously developed dynamic gas sensing setup which was attached with corrosive and non-corrosive mass flow controllers (MFCs) and data performance was recorded using Keithley 4200 A. Tedlar bags were used to get the desired concentration of gas analyte.

3 Results and discussion

3.1 Structural characterization

The structural analysis of pristine and SHI-irradiated NRs-Ni$_3$HHTP$_2$ MOF was carried out using X-ray diffraction (XRD) shown in Fig. 1a. In pristine NRs-Ni$_3$HHTP$_2$, (Fig. 1) (black) exhibits 2θ peaks at 4.5°, 9.4°, and 29° which exhibited good agreement in earlier reported data [37–39] which is consistent to (100), (020), and (311) Miller indices, respectively. The percentage of crystallinity for pristine NRs-Ni$_3$HHTP$_2$ is 48%. After C^{12+} ion irradiation, due to high energy, 2θ angle peak intensity decreases with
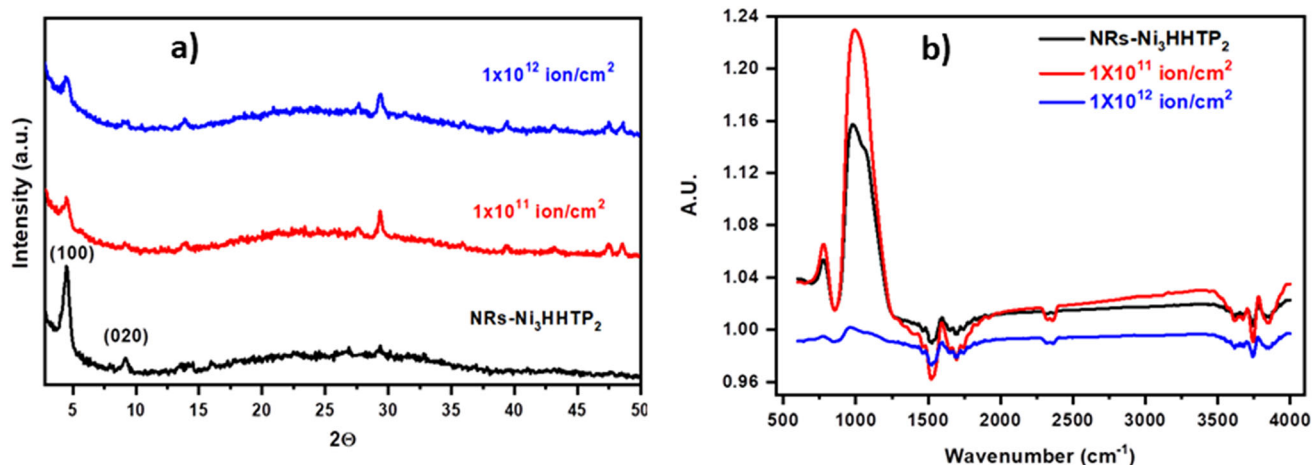
Fig. 1 **a** XRD patterns and **b** FTIR spectrum of pristine (black) and C^{12+} ion irradiation with fluence rate 1×10^{11} ion/cm^2 (red) and 1×10^{12} ion/cm^2 (blue) on NRs-Ni$_3$HHTP$_2$ MOF materials (Color figure online)

increasing fluence rate at smaller angle (5° and 9.4°), whereas at larger angle (29°) peak intensity increases [37]. The resultant distinct 2θ peaks were observed after irradiation materials at 28°. The percentage of crystallinity after C^{12+} irradiation for fluence rate 1×10^{11} (Fig. 1a (red)) and 1×10^{12} ion/cm^2 (Fig. 1, blue) was 23 and 20%, respectively. This result confirms the crystal structure collapse with increase in amorphous phase after SHI irradiation.

Besides giving crystalline structure information, the peaks of the diffraction pattern provide valuable information in other aspects of the material. The crystalline size of pristine and SHI-irradiated NRs-Ni$_3$HHTP$_2$ was calculated by using the Debye–Scherrer's formula in equation (I) at 2θ angle 4.515^0.

$$D = \frac{0.9\lambda}{\beta \cos\theta} \tag{1}$$

whereas D is crystallite size, λ is the wavelength of X-ray source radiation i.e., CuK$_\alpha$ wavelength is 1.5406 Å, β is full width at half maxima (FWHM) calculated from Gauss fitting, and θ is the Braggs angle of diffraction. Also, the dislocation density () (equation II), distortion parameter (g) (equation III), and inter-chain separation (R) (equation IV) are shown in Table 1. The crystallite size of pristine NRs-Ni$_3$-HHTP$_2$ was 170.1 Å increased with 180.4 Å and 197.1 Å with fluence rate 1×10^{11} and 1×10^{12} ion/cm^2, respectively. Also, it is interesting to see that the micro-strain increases with increasing fluence rate.

$$\delta = \frac{1}{D^2} \tag{2}$$

$$g = \frac{\beta}{\tan\theta} \tag{3}$$

$$R = \frac{5\lambda}{8\sin\theta} \tag{4}$$

3.2 Spectroscopy analysis

Fourier Transform Infrared spectroscopy (FTIR) spectrums were recorded for pristine and irradiated NRs-Ni$_3$HHTP$_2$ MOF materials in ZnSe window having range 4000−500 cm^{-1} shown in the Fig. 1b. The bands 700–900 cm^{-1} show continuous stretching containing CH$_3$-metal group due to CH$_2$ rocking vibration present in NRs-Ni$_3$HHTP$_2$ MOF. C=C stretching vibration bonds represent in between 1500 and 1580 cm^{-1}, whereas O-H stretching vibration was present in the 3200–3700 cm^{-1} range. In the case of irradiated NRs-Ni$_3$HHTP$_2$ MOF materials, some of the bands become narrow and intensity decreases, these change are attributed to the scissoring and crosslinking of material by ion beam irradiation [40]. At higher fluence (1×10^{12} ion/cm^2 (blue)), defects were created more than lower fluence (1×10^{11} ion/cm^2 (red)). This fact might be responsible for the amorphous nature of NRs-Ni$_3$HHTP$_2$ MOF materials after irradiation. Therefore, at higher fluence (1×10^{12} ion/cm^2 (blue)), low intensity represented lower absorption of light.

Table 1 XRD parameter calculated for pristine and irradiated NRs-Ni$_3$HHTP$_2$ MOF materials

| Parameter	Material								
	NRs-Ni$_3$HHTP$_2$			1×10^{11} ion/cm^2			1×10^{12} ion/cm^2		
$2\theta^0$	4.5	9.4	29	4.5	9.4	29	4.5	9.4	29
FWHM β	0.488	0.501	0.525	0.460	0.494	0.496	0.421	0.452	0.486
Crystallite size D (Å)	170.1	166.1	163.1	180.4	168.4	172.2	197.1	184.4	176.2
Dislocation density () (X10^{-21})	0.0058	0.006	0.0061	0.0055	0.0059	0.0058	0.005	0.0054	0.0056
Distortion parameter (g)	6.2037	3.0278	0.9476	5.847	2.9855	0.8953	5.352	2.7317	0.8772
Interchain separation (R)	12.2785	5.8983	1.987	12.2785	5.8983	1.987	12.2785	5.8983	1.987

3.3 Morphological studies

Scanning electron microscopy (SEM) high-magnification images were recorded before and after C$^{+\ 12}$ ion with fluence rate of 1×10^{11} and 1×10^{12} ion/cm^2 irradiation on NRs-Ni$_3$HHTP$_2$ MOF shown in Fig. 2a, b, and c, respectively. This confirms the presence of nanorods in synthesized Ni$_3$HHTP$_2$ MOF [34]. The average size of nanorods (pristine Ni$_3$HHTP$_2$, 38 nm) decreases with fluence rate i.e., C^{12+} with fluence rate 1×10^{11} and 1×10^{12} ion/cm^2, 35nm, and 28nm, respectively. This was done due to the high energetic ion passed through materials which loses electronic energy and creates defects [23]. An increased influence rate shows more clusters which are attributed to scissoring and crosslinking of material and is in good agreement with XRD and FTIR results.

Atomic force microscopy (AFM) was carried out (shown in Fig. 2d, e and f) for determination of roughness (shown in Fig. 2g, h and i) of pristine and SHI-irradiated C^{12+} with fluence rate 1×10^{11} and 1×10^{12} ion/cm^2 on NRs-Ni$_3$HHTP$_2$ MOF, respectively. The roughness was calculated by XEI image-processing software. The roughness of pristine NRs-Ni$_3$HHTP$_2$ MOF was 32.518nm and roughness after C^{12+} ion-irradiated sample was 20.053 nm and 19.475 nm with fluence rate 1×10^{11} and 1×10^{12} ion/cm^2, respectively. The decrease in surface roughness is due to discontinuous tracks and the creation of defects after irradiation of high energetic ion. Higher fluence creates more clusters in material which reduce the surface roughness as compared to lower fluence.

3.4 Optical studies

The optical absorbance spectra of pristine (black) and C^{12+}-irradiated with fluence rate 1×10^{11} ion/cm^2 (red) and 1×10^{12} ion/cm^2 (blue) on NRs-Ni$_3$HHTP$_2$ MOF shown in Fig. 3. It was observed that the pristine NR-Ni$_3$HHTP$_2$ and irradiated materials absorbance peaks are in the 400–550 nm visible wavelength range. The intensity reduction was observed in irradiated materials. The bands at $450 - 500$ nm have been frequently associated with defect absorption [41]. This was due to the creation of free radicals and ions formed by irradiation on NRs-Ni$_3$HHTP$_2$ materials. It has affected the bandgap of materials. Moreover, there is another fundamental gap present i.e., HOMO-LOMO gap. Due to defect creation minimum energy was formed in separated, uncorrelated free electron and hole, and associated with the transport of single particles in the solid, corresponding to the onset of optical absorption and formation of abound electron-hole pair or exciton. The bandgap of pristine NRs-Ni$_3$HHTP$_2$ was 3.54 eV; after C$^{+\ 12}$ ion irradiation band gap decreases. It was 3.41 eV and 3.44 eV for fluence rate of 1×10^{11} ion/cm^2 and 1×10^{12} ion/cm^2, respectively, shown in Fig. 3b-1, b-2 and b-3. This was due to the creation of pronounced coalescence phenomena in higher fluence (1×10^{12} ion/cm^2)-irradiated material [42]. It shows complementary results with structural and morphological characteristics. Due to high energy, a little bit more damage was created in the material.

The bandgap was calculated by using Tauc's equation I.
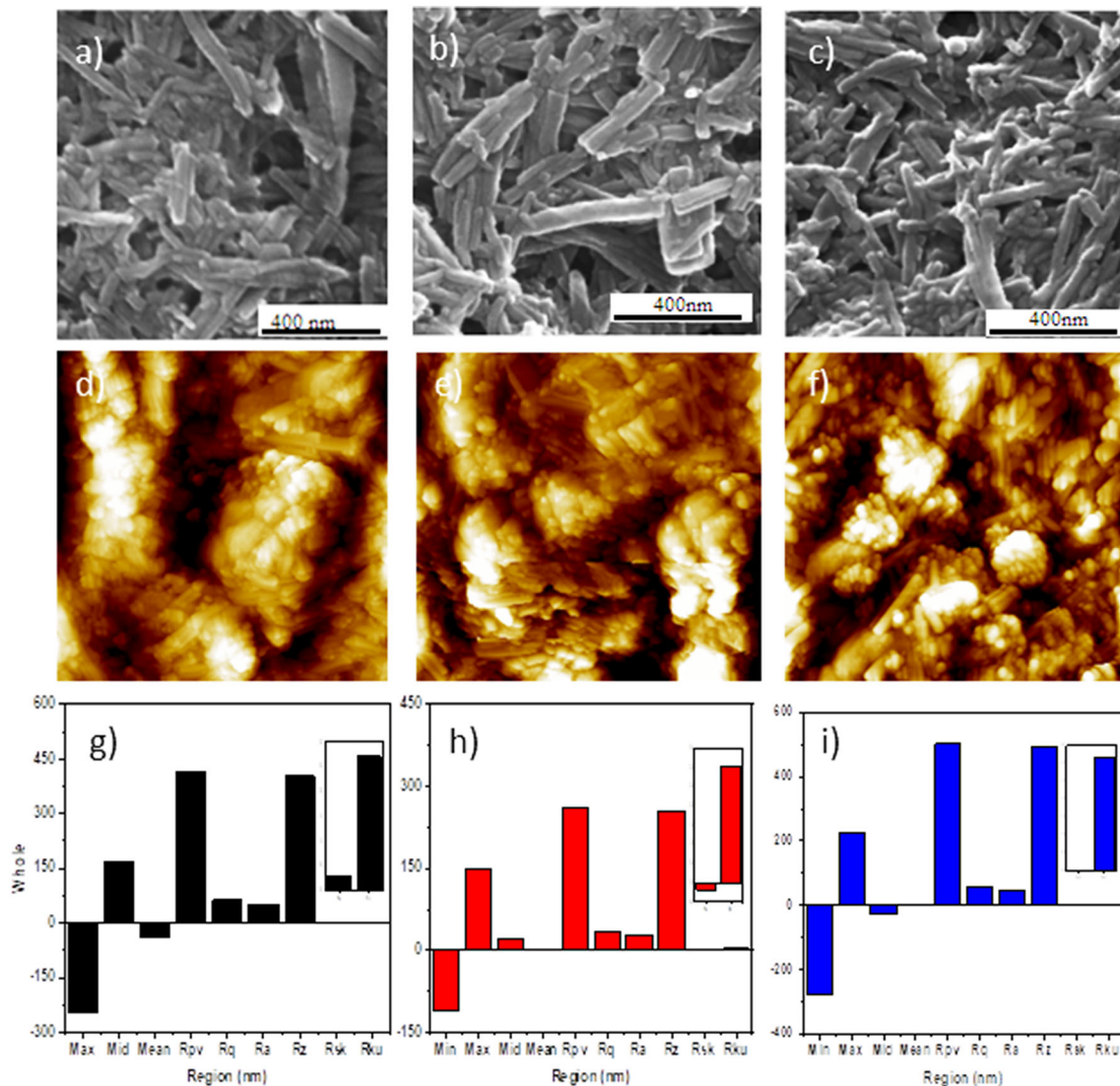
Fig. 2 SEM images (**a**, **b** and **c**) and AFM images (**d**, **e** and **f**) with surface roughness (**g**, **h** and **i**) for pristine (black) and C^{12+} ion irradiation with fluence rate 1×10^{11} ion/cm² (red) and 1×10^{12} ion/cm² (blue) on NRs-Ni₃HHTP₂ MOF materials, respectively (Color figure online)

$$\alpha = 2.303\frac{A}{d} \tag{5}$$

$$\alpha h v = A(h v - E_g)_n \tag{6}$$

where Eg is an energy bandgap of the material, α is the coefficient of absorbance calculated from equation (II), A is absorbance, and d is the thickness of deposited material.

3.5 Field effect transistor (FET) measurements

The FET measurements were carried out by measuring the output and transfer characteristics of pristine and irradiated MOFs. Output characteristics were performed by modulating drain to source voltage (V_{ds}) in the window 0 to 10 V at gate voltage (V_{gs}) 1 to 4 V for NRs-Ni₃HHTP₂ MOF shown in Fig. 4a, whereas for $C^{+ 12}$ ion-irradiated MOF materials output characteristics were performed by keeping same V_{ds} window at constant gate voltage (V_{gs}) 1 V as shown in Fig. 4b. Moreover, transfer
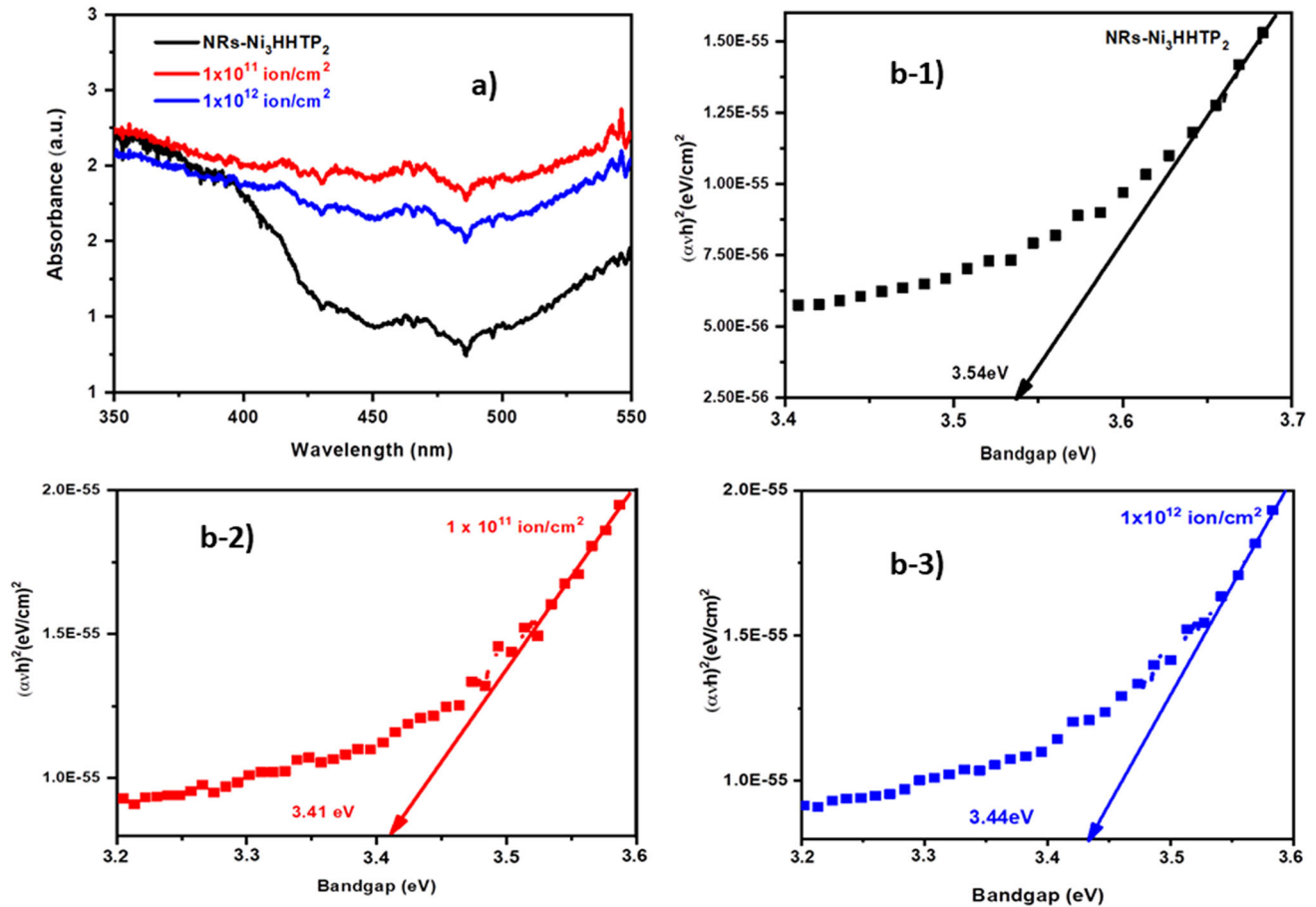
Fig. 3 a UV-Vis absorbance spectra with Tauc's plots (**b**-1, **b**-2 and **b**-3) of pristine (black) and C^{12+} irradiation with fluence rate 1×10^{11} (red) and 1×10^{12} ion/cm^2 (blue) on NRs-Ni$_3$HHTP$_2$ MOF (Color figure online)

characteristics (as shown in Fig. 4c) were measured by modulating gate to source voltage in window − 30 to 30 V_{gs} at V_{ds} = 0.5 V. Excellent ON/OFF behavior of FET was observed. The significant changes in output and transfer characteristics in pristine and SHI-irradiated device were observed. Significant enhancement in drain current (I_{ds}) was observed in SHI-irradiated MOF materials. This is due to SHI-induced defects and the creation of free radicals and ions in irradiated MOF. The SHI enhances charge transportation in irradiated MOF materials. Moreover, at higher fluence, saturation level was observed. Irradiation of higher energy creates more clusters in material which reduces the surface roughness as compared to lower fluence.

4 ChemFET sensing

The NRs-Ni$_3$HHTP$_2$ and C^{+12} ion irradiated with fluence 1×10^{11} ion/cm^2 and 1×10^{12} ion/cm^2 devices were tested in ChemFET modality for detection of SO_2 gas analytes from 1 to 0.625 ppm levels by keeping V_{gs}= 1 V and V_{ds} = 0.5 V constant as shown in Fig. 4d. The SHI irradiation was used as a tool for maximizing the surface area of the sensor. It was viable approach for increasing the efficacy of sensing. This means that surfaces with higher porosity offer a greater number of sites for the adsorption of toxic gas molecules, increasing the number of reactions with sensor molecules. Accordingly, the porosity of the sensor surface has a direct relation with the sensor performance, sensor sensitivity, and sensor response. Reversible ChemFET sensing was observed for SO_2 gas analytes. It was showing remarkable dynamic sensing response against SO_2 analytes. The significant improvement in
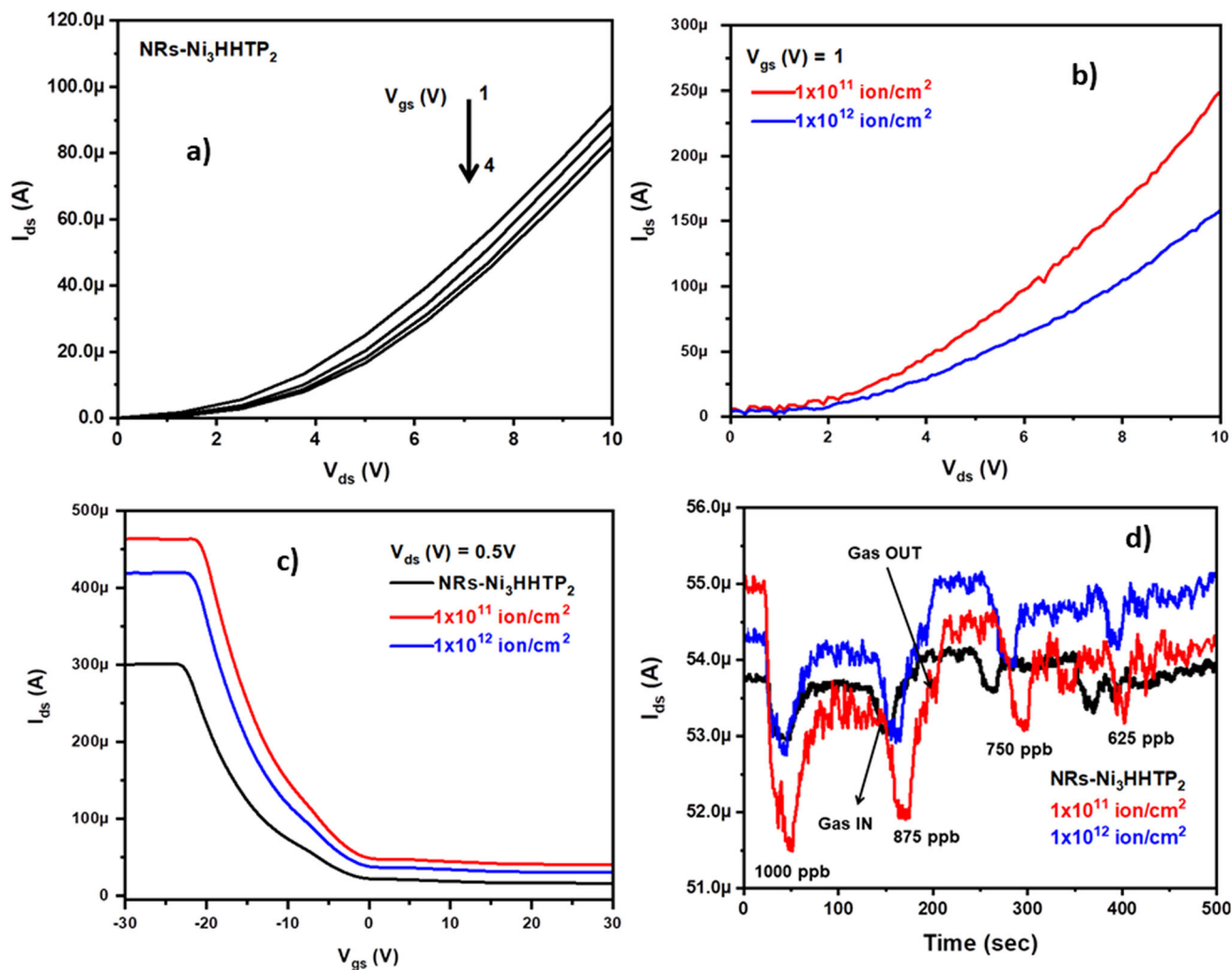
Fig. 4 FET measurements i.e., output characteristics for **a** NRs-Ni$_3$HHTP$_2$ MOF and **b** after C$^{+\ 12}$ ion irradiation on MOF material, whereas **c** transfer characteristics and **d** ChemFET sensing for SO$_2$ analytes

the sensing performance was observed in case of SHI-irradiated MOF. The enhancement in sensing performance may be attributed to the increased active sites for SO$_2$ adsorption on MOF after SHI irradiation. The statistical approach for calculating regression coefficient for SO$_2$ analytes was adopted by using linear regression equations and normalized current responses are plotted against gas concentrations for pristine and SHI-irradiated MOF as shown in Fig. 5a. For NRs-Ni$_3$HHTP$_2$ MOF linear regression equation was y = 0.0018x -1.009 with R square 0.785. Moreover, for SHI-irradiated MOF (C$^{+\ 12}$ ion-irradiated MOF with fluence 1×10^{11} ion/cm^2 and 1×10^{12} ion/cm^2) linear regression equation was y = 0.0018x − 0.675 with R square 0.931 and y = 0.0014x − 0.588 with R square 0.9142, respectively. The C$^{+\ 12}$ ion-irradiated MOF with fluence 1×10^{11} ion/cm^2 shows excellent (0.931) regression coefficient. On that line, repeatability was tested for 1 ppm using C$^{+\ 12}$ ion-irradiated MOF with fluence 1×10^{11} ion/cm^2 as shown in Fig. 5-b and it shows excellent repeatability.

The standard error bar is one of the crucial points in sensor properties. The calibration plot is shown in Fig. 5-c. It exhibited lower deviation at higher concentration of SO$_2$ analytes, whereas higher deviations at lower concentrations. The cross-selectivity performance of SHI-irradiated MOF for various gas analytes i.e., SO$_2$, NO$_2$, NH$_3$, CO, and CH$_4$ were also investigated. It shows good selectivity towards SO$_2$ analytes as shown in Fig. 5-d. The SHI-irradiated MOF (C$^{+\ 12}$ ion irradiated with fluence 1×10^{11} ion/
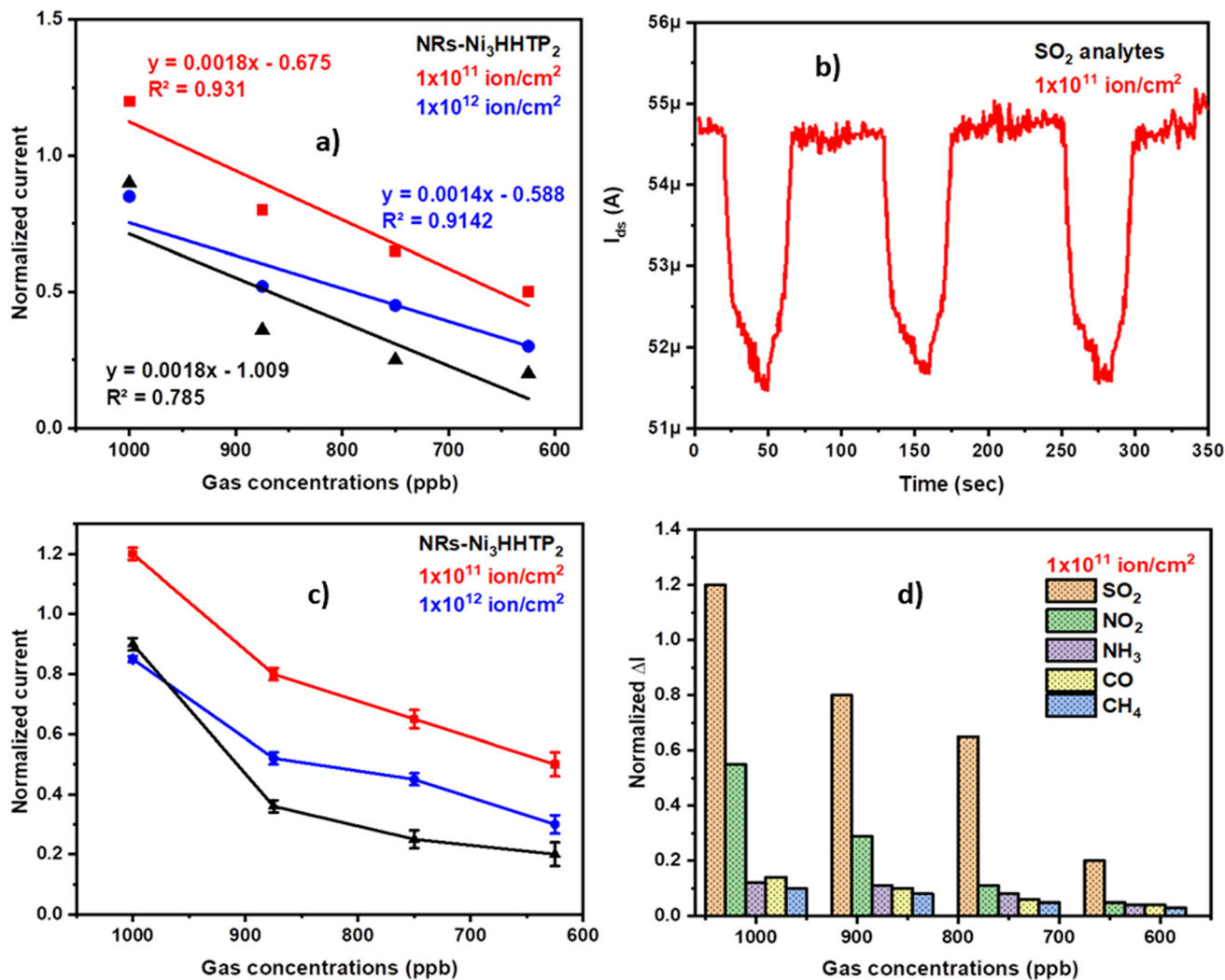
Fig. 5 **a** plot of concentration versus normalized current with R-squared value, **b** repeatability for SO_2 analytes, **c** standard error bar, and **d** selectivity performance of C^{+12} ion irradiation with fluence 1×10^{11} ion/cm^2 sensor towards various gases

cm^2 sensor) exhibits improved selectivity due to increased stacking coefficient for SO_2 adsorption in sensing material. The long-term stability was also investigated continuously for 60 days on pristine as well as irradiated sensors as shown in supporting information (SI) figure S1-1. The SHI-irradiated MOF exhibited degradation after 25 days. It might be because of creation of more number of defects due to SHI irradiation. The low-energy SHI-irradiated MOF showed better results than higher-energy SHI-irradiated MOF in terms of long-term stability. The most important parameters in the sensor are response and recovery time, lower detection limit, and operating temperature. Table 2 shows comparison of above-mentioned sensing parameters of earlier reported work and present work. It can be concluded that

present work shows better results as compared to earlier reported work. It shows excellent response and recovery time i.e., 20 and 23 s for 1 ppm SO_2 concentration at room temp (RT) with a lower detection limit of 0.625 ppm.

4.1 Sensing mechanism

The sensing mechanism is the key factor to understand the sensing behavior of materials. To understand the sensing mechanism, we have calculated bandgap using Tauc's plot as shown in Fig. 3-b (1,2 and 3). It shows decrease in banggap after SHI irradiation. After SHI irradiation, defects, free radicals, and ions were created on sites of materials. These

Table 2 Presented work sensing parameters compared with the recent works of literature

Material	Response/recovery time (s)	Lower detection limit	Operating temp.	Ref.
S-doped SnO_2	30 /50 for 100 ppm	10 ppm	180 °C	[43]
NiO ZnO nanodisks	52/41 for 20 ppm	3 ppm	240 °C	[13]
$Ru/Al_2O_3/ZnO$	$\sim 60/\sim 360$	5 ppm	350 °C	[44]
$AuNPs-SnO_2$	34/14 for 20 ppm	0.5ppm	200 °C	[45]
NRs-Ni_3HHTP_2 irradiation with $C^{+\ 12}$ at fluence 1×10^{11} ion/cm^2	$\sim 20/\sim 23$ for 1ppm	0.625ppm	RT	Present work
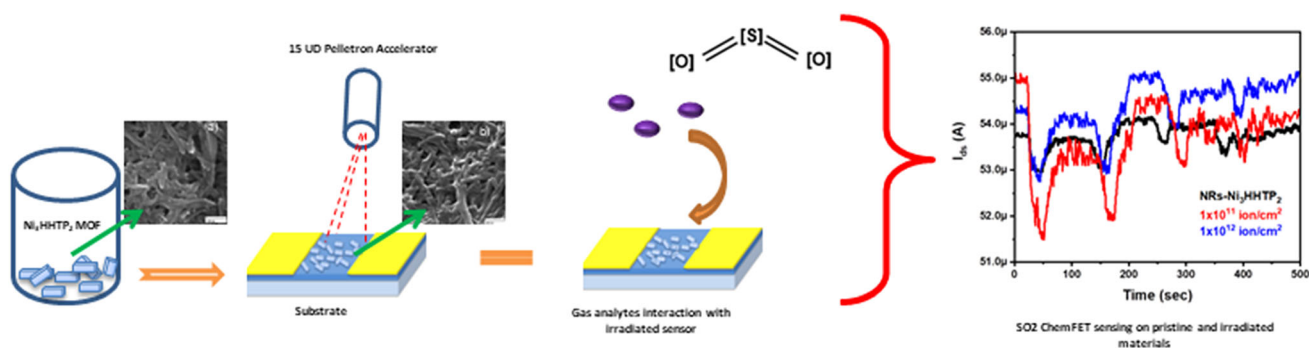
Fig. 6 schematic for material synthesis, ion irradiation, and sensing mechanism

defects act as an electron trapper with adsorption of the oxygen species from gas analytes. Moreover, these defects are responsible for adsorbing oxygen species and creating oxygen ions thereby preventing electron-hole recombination rate [46]. This was responsible for decreasing drain current after exposing to gas analyte as shown in Fig. 6.

5 Conclusions

The NRs-Ni_3HHTP_2 MOFs were successfully synthesized by the chemical method. The SHI irradiation C^{12+} with fluence 1×10^{11} ion/cm^2 and 1×10^{12} ion/cm^2 have induced changes in structural, spectroscopic, morphological, optical, and FET properties of NRs-Ni_3HHTP_2 MOFs. The NRs-Ni_3HHTP_2 MOF was amorphized after SHI irradiation which was confirmed by XRD. The XRD pattern exhibits the creation of defects in irradiated materials. The size of NRs-Ni_3HHTP_2 MOF decreases with decreasing the surface roughness and forms a cluster in irradiated materials which was confirmed from surface morphology by SEM and AFM. The decrease in surface

roughness was attributed to discontinuous tracks, which lead to amorphization. The drain current of NRs-Ni_3HHTP_2 MOFs-based FET was enhanced due to the trapping of free mobile carriers after the SHI irradiations. The SHI-induced surface defects in NRs-Ni_3HHTP_2 MOFs were responsible for enhancing sensing properties. It shows excellent response and recovery time i.e., 20 and 23 s for 1 ppm SO_2 concentration at room temp (RT) with a lower detection limit of 0.625 ppm. Therefore, it can be concluded that SHI-irradiated NRs-Ni_3HHTP_2 MOFs showed improved material properties which were responsible for enhancing sensing properties.

References

1. G.A. Bodkhe et al., Field effect transistor based on proton conductive metal organic framework (CuBTC). J. Phys. D: Appl. Phys. **52**(33), 335105 (2019)

2. D. Wang, D. Jana, Y. Zhao, Metal–Organic Framework Derived Nanozymes in Biomedicine. Acc. Chem. Res. **53**(7), 1389–1400 (2020)

3. G.A. Bodkhe et al., Selective and sensitive detection of lead Pb(II) ions: Au/SWNT nanocomposite-embedded MOF-199. J. Mater. Sci. **56**(1), 474–487 (2020)

4. A. Rashti et al., Tuning MOF-derived Co3O4/NiCo2O4 nanostructures for high-performance energy storage. ACS Appl. Energy Mater. **4**(2), 1537–1547 (2021)

5. N. Ingle et al., Sulfur dioxide (SO_2) detection using composite of Nickel benzene carboxylic (Ni_3BTC_2) and OH-functionalized single walled carbon nanotubes (OH-SWNTs). Front. Mater. **7**, 93 (2020)

6. M. Dinari, F. Jamshidian, Preparation of MIL-101-NH2 MOF/triazine based covalent organic framework hybrid and its application in acid blue 9 removals. Polymer **215**, 123383 (2021)

7. M. Mahadik et al., EDTA modified PANI/GO composite based detection of Hg(II) ions. Front. Mater. **7**, 81 (2020)

8. H. Nazemi et al., Advanced micro-and nano-gas sensor technology: a review. Sensors **19**(6), 1285 (2019)

9. A. Nowoświat, L. Dulak, Impact of cement dust pollution on the surface of sound-absorbing panels on their acoustic properties. Materials **13**(6), 1422 (2020)

10. P.W. Sayyad et al., Chemiresistive SO_2 sensor: graphene oxide (GO) anchored poly (3,4-ethylenedioxythiophene): poly (4styrenesulfonate)(PEDOT: PSS). Appl. Phys. A **126**(11), 1–8 (2020)

11. Y. Wu et al., The high-resolution estimation of sulfur dioxide (SO2) concentration, health effect and monetary costs in Beijing. Chemosphere **241**, 125031 (2020)

12. A. Yang et al., Single ultrathin WO3 nanowire as a superior gas sensor for SO2 and H2S: Selective adsorption and distinct IV response. Mater. Chem. Phys. **240**, 122165 (2020)

13. Q. Zhou et al., High sensitive and low-concentration sulfur dioxide (SO2) gas sensor application of heterostructure NiO-ZnO nanodisks. Sens. Actuators B **298**, 126870 (2019)

14. V. Kumar, D.R. Roy, Single-layer stanane as potential gas sensor for NO2, SO2, CO2 and NH3 under DFT investigation. Physica E **110**, 100–106 (2019)

15. N. Ingle et al., A chemiresistive gas sensor for sensitive detection of SO 2 employing Ni-MOF modified–OH-SWNTs and–OH-MWNTs. Appl. Phys. A **127**(2), 1–10 (2021)

16. M. Tchalala et al., Fluorinated MOF platform for selective removal and sensing of SO_2 from flue gas and air. Nat. Commun. **10**(1), 1–10 (2019)

17. A.S. El-Said et al., Tuning tailored single-walled carbon nanotubes by highly energetic heavy ions. Phys. Rev. Appl. **13**(4), 044073 (2020)

18. H. Gupta et al., Defect-induced photoluminescence from gallium-doped zinc oxide thin films: influence of doping and energetic ion irradiation. Phys. Chem. Chem. Phys. **21**(27), 15019–15029 (2019)

19. P. Esquinazi et al., Induced magnetic ordering by proton irradiation in graphite. Phys. Rev. Lett. **91**(22), 227201 (2003)

20. A. Krasheninnikov, K. Nordlund, Ion and electron irradiation-induced effects in nanostructured materials. J. Appl. Phys. **107**(7), 3 (2010)

21. I.I.I. Wood et al., Perspectives on the relationship between materials chemistry and roll-to-roll electrode manufacturing for high-energy lithium-ion batteries. Energy Storage Mater. **29**, 254–265 (2020)

22. S. Raghuvanshi et al., Dual control on structure and magnetic properties of Mg ferrite: role of swift heavy ion irradiation. J. Magn. Magn. Mater. **471**, 521–528 (2019)

23. A. Ratan et al., Enhanced electrical properties of few layers MoS2-PVA nanocomposite film via homogeneous dispersion and annealing effect induced by 80 MeV Carbon6 + swift heavy ion irradiation. Mater. Sci. Semicond. Process. **108**, 104877 (2020)

24. M. Karlušić et al., Nanopatterning surfaces by grazing incidence swift heavy ion irradiation. Appl. Surf. Sci. **541**, 148467 (2021)

25. R. Singh et al., Tuning of defects induced visible photoluminescence by swift heavy ion irradiation and thermal annealing in zinc oxide films. Radiat. Phys. Chem. **183**, 109400 (2021)

26. J. Zeng et al., Graphene electrical properties modulated by swift heavy ion irradiation. Carbon **154**, 244–253 (2019)

27. N. Manikanthababu et al., Swift heavy ion irradiation-induced modifications in the electrical and surface properties of β-Ga2O3. Appl. Phys. Lett. **117**(14), 142105 (2020)

28. H.K. Patil et al., Reinforcement of polyaniline and poly-(o-toluidine) with SWNTs and tuning of their physicochemical properties by heavy ion beams. Appl. Phys. A **124**(7), 491 (2018)

29. H.K. Patil, et al., Spectroscopic investigations upon 100 MeV oxygen ions irradiation on polyaniline and poly-o-tolui-dine. In: AIP Conference Proceedings. 2018. AIP Publishing LLC

30. O. Ochedowski et al., Radiation hardness of graphene and MoS2 field effect devices against swift heavy ion irradiation. J. Appl. Phys. **113**(21), 214306 (2013)

31. T. Bolse, H. Paulus, W. Bolse, Swift heavy ion induced dewetting of metal oxide thin films on silicon. Nucl. Instrum. Methods Phys. Res. Sect. B **245**(1), 264–268 (2006)

32. R. Dutta, A. Kumar, 100 MeV O7+ ion irradiation induced electrochemical enhancement in NiBTC metal-organic framework based composite polymer electrolytes incorpo-rated with ionic liquid. Mater. Res. Exp. **6**(8), 085305 (2019)

33. P.W. Sayyad et al., Tuning the properties of Fe-BTC metal-organic frameworks (MOFs) by swift heavy ion (SHI) irra-diation. Radiat Effects Defects Solids (2020). https://doi.org/10.1080/10420150.2020.1825958

34. N. Ingle et al., ChemFET Sensor: nanorods of nickel-substi-tuted metal–organic framework for detection of SO_2. Appl. Phys. A **126**(9), 1–9 (2020)

35. T.D. Malouff et al., Carbon ion therapy: a modern review of an emerging technology. Front. Oncol. **10**, 82 (2020)

36. K. Datta et al., Organic field-effect transistors: predictive control on performance parameters. J. Phys. D: Appl. Phys. **46**(49), 495110 (2013)

37. M. Ko et al., Employing conductive metal–organic frame-works for voltammetric detection of neurochemicals. J. Am. Chem. Soc. **142**(27), 11717–11733 (2020)

38. M.K. Smith et al., Direct self-assembly of conductive nanorods of metal–organic frameworks into chemiresistive devices on shrinkable polymer films. Chem. Mater. **28**(15), 5264–5268 (2016)

39. M.K. Smith, K.A. Mirica, Self-organized frameworks on textiles (SOFT): conductive fabrics for simultaneous sensing, capture, and filtration of gases. J. Am. Chem. Soc. **139**(46), 16759–16767 (2017)

40. J. Ram et al., Ion beam engineering in WO3-PEDOT: PSS hybrid nanocomposite thin films for gas sensing measurement at room temperature. Inorg. Chem. Commun. **119**, 108000 (2020)

41. H. Xu et al., Ag/Ag2S nanoparticle-induced sensitization of recovered sulfur-doped SnO_2 nanoparticles for SO_2 detection. ACS Appl. Nano Mater. **3**(8), 8075–8087 (2020)

42. R.U. Mene, M.P. Mahabole, R.S. Khairnar, Surface modified hydroxyapatite thick films for CO_2 gas sensing application: effect of swift heavy ion irradiation. Radiat. Phys. Chem. **80**(6), 682–687 (2011)

43. H. Xu et al., Ag/Ag2S nanoparticle-induced sensitization of recovered sulfur-doped SnO_2 nanoparticles for SO_2 detection. ACS Appl. Nano Mater. **8**, 8075–8087 (2020)

44. Y. Liu et al., An integrated micro-chip with Ru/Al2O3/ZnO as sensing material for SO2 detection. Sens. Actuators B **262**, 26–34 (2018)

45. L. Liu, S. Liu, Oxygen vacancies as an efficient strategy for promotion of low concentration SO2 gas sensing: the case of Au-modified SnO2. ACS Sustain. Chem. Eng. **6**(10), 13427–13434 (2018)

46. S.K. Lim et al., Preparation of ZnO nanorods by microemulsion synthesis and their application as a CO gas sensor. Sens. Actuators B **160**(1), 94–98 (2011)